Temperature effects on the electrodeposition of semiconductors from a weakly coordinating solvent

Alexander W. Black [a], Wenjian Zhang [a], Yasir J. Noori [b], Gillian Reid [a], Philip N. Bartlett [a,*]

[a] School of Chemistry, University of Southampton, Southampton SO17 1BJ, UK
[b] School of Electronics and Computer Science, University of Southampton, Southampton SO17 1BJ, UK

ABSTRACT

Temperature is an important variable in electrochemistry, increasing the operating temperature has the capacity to provide significant increases in mass transport and electron transfer rates. In the case of electrodeposition, it can also allow the deposition of crystalline material which would otherwise be amorphous when grown at lower temperatures. In this work we exploit a high boiling point, weakly coordinating solvent, o-dichlorobenzene, to electrodeposit the p-block semiconductors antimony and antimony telluride at temperatures up to 140 °C. The effect of the temperature on the morphology and crystallinity of the deposits is investigated using scanning electron microscopy, X-ray diffraction, Raman spectroscopy and optical microscopy. An attempt is also made to rationalise the role of temperature in electrodeposition and its influence on the aforementioned properties.

1. Introduction

Weakly coordinating solvents (WCSs) are of interest for semiconductor electrodeposition because they are poor Lewis bases and so do not interact strongly with the metal precursor dissolved in solution. This is important in the electrodeposition of alloys and compounds because solvent interference can disrupt the speciation of the metal complex and cause variations in the deposition potential, electron transfer kinetics and mass transport of the metals. This can greatly complicate the process of achieving co-deposits with a controlled stoichiometry.

Recently, dichloromethane (CH_2Cl_2, DCM) has been used as a WCS to successfully electrodeposit various p-block metal semiconductors, such as Bi_2Te_3 [1], HgTe [2], and $Ge_2Sb_2Te_5$ [3]. However, DCM has a low boiling point and high volatility, which can make it practically challenging to use, and also restricts experiments to near room temperature. In a recent study, o-dichlorobenzene (oDCB) was identified as a promising WCS for the electrodeposition of semiconductors [4]. oDCB was shown to behave electrochemically similarly to DCM, but with a boiling point of 180 °C, much greater than the 40 °C for DCM, therefore allowing the possibility of electrodeposition at elevated temperatures from a weakly coordinating solvent.

Electrodeposition of semiconductors at elevated temperatures is interesting because it can improve the material properties, such as crystallinity, of the resulting deposit. Examples of this can be found in the literature for a variety of materials. Si was electrodeposited in a crystalline form when heated to 80 °C in propylene carbonate [5]. Wu *et al.* reported the electrodeposition of crystalline Re-Ir-Ni alloys from water at 70 °C [6], and it was also possible to electrodeposit crystalline MoS_2 at 100 °C from ionic liquids [7], all of which were amorphous when grown at room temperature. Furthermore, where a semiconductor deposits amorphously at room temperature it would commonly be annealed to render it crystalline [8]. Electrodeposition at elevated temperatures (of a material that grows in an amorphous form at room temperature) would remove the need for annealing *post hoc,* and is therefore an attractive capability in the field. The crystallinity of the material is an important consideration in the applications of semiconductor devices because it can have significant consequences for its electron transport properties.

Thin layers of Sb are of interest as field effect transistors [9], and Sb_2Te_3 is a promising p-type thermoelectric material [10]. Both of these applications require the presence of crystalline material. Elemental Sb and Sb_2Te_3 have both previously been shown to deposit amorphously or partially crystalline from DCM at room temperature [11,12], and so are good candidates to investigate the role temperature has in the electrodeposition process. In the present work, antimony and antimony telluride were electrodeposited onto TiN from oDCB at various temperatures between 25 °C and 140 °C. The effect

* Corresponding author.
E-mail address: p.n.bartlett@soton.ac.uk (P.N. Bartlett).

of temperature on the resulting deposit was monitored using scanning electron microscopy (SEM), X-ray diffraction (XRD), Raman spectroscopy and optical microscopy. A transition from amorphous to crystalline was indeed observed for both Sb and Sb_2Te_3 when depositing at higher temperatures. The deposits also became smoother and more uniform with increasing temperature. However, the temperature 'window' for electrodeposition is limited by the stability of the precursors, which appeared to decompose at the highest temperatures.

2. Experimental

2.1. Chemicals

o-dichlorobenzene, $C_6H_4Cl_2$ (oDCB) (>99% Sigma-Aldrich, UK) was dried and degassed by refluxing with CaH_2 under a dinitrogen atmosphere followed by distillation, and was stored in an ampoule under an inert atmosphere of N_2. The water content in the solvent was measured with Karl–Fischer titration (KF 899 Coulometer Metrohm, UK), averaging less than 30 ppm across batches of solvent. Tetrabutylammonium chloride, $[N^nBu_4]Cl$ (>99% Sigma-Aldrich, UK) was dried by heating at 100 °C under vacuum for several hours. Decamethylferrocene, $[\{C_5(CH_3)_5\}_2Fe]$ (DMFc) (>97% Sigma-Aldrich, UK) was purified by sublimation. Tetrabutylammonium tetrachloroantimonate(III), $[N^nBu_4][SbCl_4]$ and tetrabutylammonium hexachlorotellurate(IV), $[N^nBu_4]_2[TeCl_6]$ were prepared using methods previously described in the literature [13]. Antimony(III) telluride lumps (99.999% Alfa Aesar, UK) for the EDX standard were used as received. All solvents and reagents were stored in a dry, N_2 purged glovebox.

2.2. Electrodes

A Pt mesh was used as the counter electrode, the reference electrode was a custom made Ag/AgCl immersed in a storage solution of 100 mM $[N^nBu_4]Cl$, separated from the electrolyte by a porous glass frit. Substrates for electrodeposition were 20 × 10 mm thin film TiN on Si chips with a 4 mm diameter exposed area. The substrates were manufactured using typical microfabrication methods in a manner that has been described previously [11]. Briefly, 200 nm thick layer TiN was plasma sputtered onto Si/SiO_2 wafers followed by the sputtering of a 200 nm SiO_2 layer. The top SiO_2 layer was patterned by photolithography and half etched by plasma dry etching and removed completely using a buffered oxide etchant. A Cr/Au 10/190 nm layer was deposited via thermal evaporation onto the contact area to minimise contact resistance.

2.3. Equipment

A Philips XL30 ESEM scanning electron microscope was used to image the deposits. Elemental composition was determined by energy dispersive X-ray spectroscopy using a Thermo Scientific NORAN System 7 X-ray Microanalysis System at a working distance of 10 mm and an accelerating voltage of 10 kV. Grazing incidence X-ray diffraction patterns were collected using a Rigaku SmartLab thin film (9 kW) diffractometer (Cu-Kα, λ = 1.5418 Å) with a parallel incident beam at an angle of 1° and Hypix-3000 detector. Phase identification was performed with the Rigaku PDXL-2.8.4 package (Rigaku Corporation, Japan) and diffraction patterns from the Inorganic Crystal Structure Database (ICSD, FIZ Karlsruhe GmbH, Germany). Instrumental line broadening was corrected using a LaB_6 external standard. Raman spectroscopy was performed using a Renishaw InVia microscope coupled to a 785 nm laser at a power of 0.1 mW. An exposure time of 15 s was used with 10 accumulations. Data was collected with WiRE 4.1 software (Renishaw plc, UK). Optical microscopy was performed using a Nikon LV100ND (Nikon Metrology, UK) in bright field mode with episcopic illumination. Images were captured using NIS Elements software (Nikon Instruments, UK) with added EDF module. Mass spectrometry was performed using a Waters Acquity Platform UHPLC-MS with electrospray ionisation in MeCN. All data was analysed with Origin 2020 (Origin Lab, USA).

2.4. Electrochemical measurements

All glassware was cleaned by soaking in Decon 90 (Decon Laboratories Ltd., UK) for at least 24 h, followed by rinsing with ultrapure water, 0.055 μS cm^{-1} and then dried in an oven for a further 24 h. Experiments at elevated temperatures necessitated a novel cell design. The potential of the reference electrode is temperature sensitive and so a 'non-isothermal' cell was used based on an approach taken by Weaver [14], fabricated in the School of Chemistry glass workshop at the University of Southampton. In this design the cell is composed of two compartments, one containing the WE and the CE that is heated, and a separate compartment housing the RE that remains at room temperature. A schematic is given in the SI. The main compartment was jacketed with silicone oil (Alfa Aesar, UK). Heat was provided by a RCT digital hot plate (IKA, UK) with the temperature in the cell controlled with a PT1000.90 temperature sensor (IKA, UK). The WE and CE were fed through GL14 ports, and sealed with silicone rubber sealing rings with a PTFE washer (DWK Life Sciences, Germany) held in place with apertured PBT screw caps (DWK Life Sciences, Germany). The electrolyte was prepared in a glovebox (Belle Technology, UK) under an inert atmosphere of N_2 in the presence of <5 ppm O_2 and H_2O. The cell was then loaded, sealed, removed from the glovebox and connected to an Ar gas line, with a gas bubbler fitted to the cell. Ar was flowed whilst heating to maintain an inert atmosphere, and then switched off during experiments. Measurements were performed with a PGSTAT μIII (Metrohm Autolab, UK) potentiostat. Data was recorded with NOVA 1.11 (Metrohm Autolab, UK).

3. Results and discussion

3.1. Temperature effects on redox potential

The 'non-isothermal' cell design employed here ensures that the potential of the RE remains unaffected by any enforced changes in temperature and therefore that good control over the potential can be maintained during electrodeposition experiments at elevated temperatures. Furthermore, in a non-isothermal cell design the change in the measured redox potential of a couple with temperature, $dE_{1/2}/dT$, consists of three components:

$$\frac{dE_{1/2}}{dT} = \frac{dE_{tlj}}{dT} + \frac{dE_T}{dT} + \frac{dE_{rc}}{dT} \tag{1}$$

where E_{tlj} is the thermal liquid junction potential (tlj), arising because of the potential difference between heated and unheated sections of the cell and E_T is the potential difference caused by the Thompson effect; a thermoelectric effect arising from the temperature differential in the working electrode wire [14–16]. E_{rc} is then the contribution from the redox couple under investigation. The tlj has been measured in aqueous electrolytes using a similar non-isothermal cell arrangement and values were generally less than 25 μV K^{-1} [15]. Similar information is not available for non-aqueous electrolytes but the magnitude can be assumed to be similar. The Thompson coefficient for Pt is 6 μV K^{-1} [14], suggesting that shifts associated with these effects will be minimal. Since $\Delta G = nFE$,

$$nFE = T\Delta S - \Delta H \tag{2}$$

and if E_{tlj} and E_T are negligible then [16]

$$\frac{dE_{1/2}}{dT} = \frac{\Delta S_{rc}}{nF} \tag{3}$$

It important to confirm that the design of our cell is successful at containing the heating to the main compartment and that E_{tlj} and E_T can be ignored. This was achieved with the use of decamethylferrocene (DMFc) as a model redox couple. The redox potential of DMFc was measured as a function of temperature in oDCB between 25 and 120 °C and a representative plot of $E_{1/2}$ vs. T is given in Fig. 1. Representative voltammograms are also shown in Fig. S2. A good linear relationship between redox potential and temperature is observed, and the resulting ΔS_{rc} can be found in Table 1. ΔS_{rc} can also be predicted using the Born equation [16]:

$$\Delta S_{rc} = -\frac{N_A e^2}{8\pi \varepsilon_0 \varepsilon_r r_i} \frac{\partial \ln \varepsilon_r}{\partial T} \left(z_{ox}^2 - z_{red}^2 \right) \tag{4}$$

where N_A is Avogadro's number, e is the elementary charge, ε_0 is the permittivity of free space, ε_r is the dielectric constant, r_i is the radius of the species, $\partial \ln \varepsilon_r / \partial T$ is the change in dielectric constant of the solvent with temperature and z is the charge of the oxidised and reduced species. The van der Waals radius, from the van der Waals volume, was used as r_i for DMFc with a value of 0.42 nm [17]. It was also assumed that the radius is the same in the oxidised and reduced forms [18]. ε_r of oDCB at 25 °C is 9.9, and $\partial \ln \varepsilon_r / \partial T$ was taken as -0.00297, both from Ref. [19]. As can be seen, there is good agreement between theory and experiment, indicating that the cell is truly 'non-isothermal'. Although, such close agreement is likely to be fortuitous, since there are uncertainties in both r_i and $\partial \ln \varepsilon_r / \partial T$. No literature measurements could be found for oDCB, although Noviandri et al. reported values in dichloromethane and 1,2-dichloroethane, two similarly weakly coordinating solvents, of 13 J K^{-1} mol^{-1} and 59 J K^{-1} mol^{-1} respectively [20]. These are of a similar order to the value obtained here, and support the conclusions from the Born estimate.

3.2. Antimony electrodeposition

Fig. 2 shows a voltammogram of 3 mM [N^{n}Bu$_4$][SbCl$_4$] at a TiN electrode at 25 °C. Scanning negatively, a reduction current is observed, beginning at approx. -1.2 V vs. Ag/AgCl which can be attributed to the electrodeposition of Sb. This results in a peak at ca. -1.6 V, followed by the onset of electrolyte breakdown at -2 V. On the return scan the current crosses the x-axis at -0.5 V and a small amount of stripping occurs. There are no major changes to the voltammetry on subsequent scans.
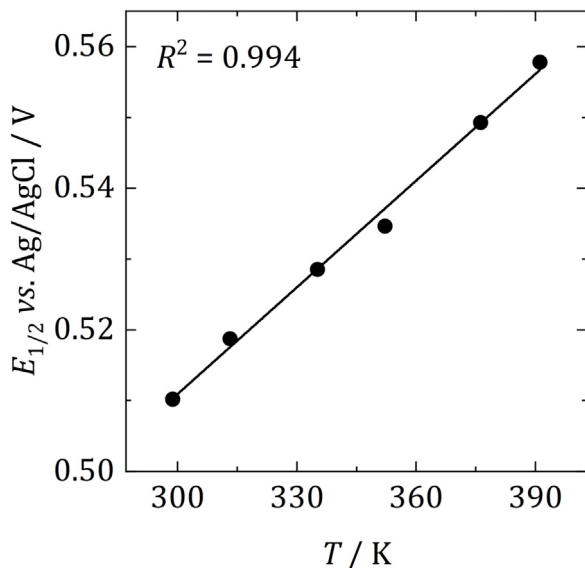
Table 1

Temperature dependence of the redox potential of DMFc in oDCB and associated experimental and theoretical reaction entropies. Experimental values are the average of three repeats with the error the standard deviation.

	d $E_{1/2}$ / dT / mV K^{-1}	ΔS_{rc}(exp) / J K^{-1} mol^{-1}	ΔS_{rc}(calc) / J K^{-1} mol^{-1}
oDCB	0.50(3)	48(3)	49
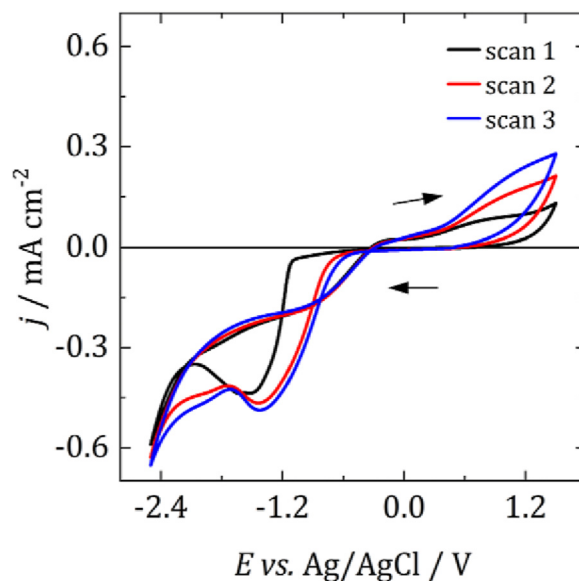
Fig. 2. Voltammograms of 3 mM [N^{n}Bu$_4$][SbCl$_4$] and 100 mM [N^{n}Bu$_4$]Cl at a 4 mm dia. TiN WE in oDCB at 25 °C. Scan swept from 0.5 V vs. Ag/AgCl at 100 mV s^{-1} in the direction indicated by the arrows. CE: Pt mesh, RE: Ag/AgCl.

Depositions were performed at -1.8 V, corresponding approximately to the peak in the voltammogram above. Depositions were performed with a cut-off charge, which corresponded to the charge passed after a 30 min deposition at 25 °C. A voltammogram of [N^{n}Bu$_4$][SbCl$_4$] was also recorded at 100 °C (see Fig. S3) to assess any changes in the crossover potential for Sb deposition and stripping. The potential shifted by less than 100 mV, and so it can be assumed that the overpotential for deposition remained constant with temperature.

SEM images of the deposits collected at each temperature are shown in Fig. 3. At 25 °C, the deposits grow as a compact film with clumps of Sb dispersed over the surface. As the temperature increases, the film becomes smooth and homogeneous. Finally at 140 °C, Sb grows primarily as small islands on top of the electrode. This therefore shows a significant improvement in the quality of the morphology of the film, simply by increasing the deposition temperature and without the need for additives.

The average deposition current density, $j_{d,av}$, was also calculated for the depositions at each temperature. The average deposition current density gives an indication of the average rate of mass growth during the deposition process. More common calculations of thickness were avoided because they carry with them assumptions, e.g. 100% Faradaic efficiency, or a compact film, that could not be verified here. Table 2 shows $j_{d,av}$ for the deposits at each temperature. The rate of deposition increases with temperature up to 120 °C, as would be expected since the rate of mass transport increases. However, this then decreases for the deposit collected at 140 °C. It is possible this is caused by a decrease in the concentration of the Sb precursor and this is discussed further below.
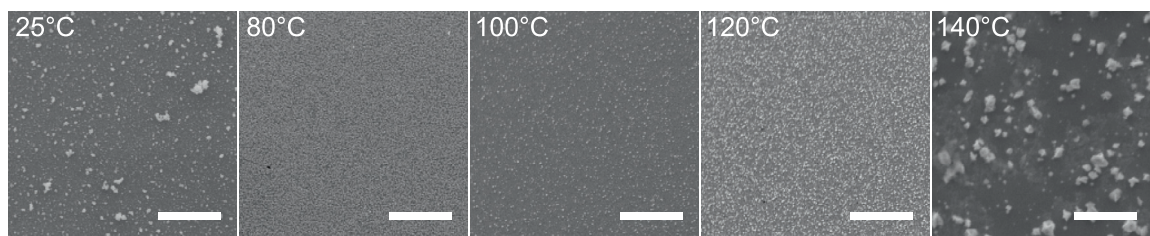

Fig. 1. Representative plot of the variation of $E_{1/2}$(DMFc) with temperature in oDCB.

Fig. 3. SEM images of Sb deposited at varying temperatures onto a TiN substrate from oDCB containing 3 mM $[N^nBu_4][SbCl_4]$. Scale bar represents 10 μm.

Table 2
Average deposition current density and quantitative XRD analysis for the deposition of Sb at various temperatures onto a 4 mm dia. TiN substrate from oDCB containing 3 mM $[N^nBu_4][SbCl_4]$. [a]Obtained using the Scherrer method. [b]Obtained using the Halder-Wagner method. [c]ICSD 64695.

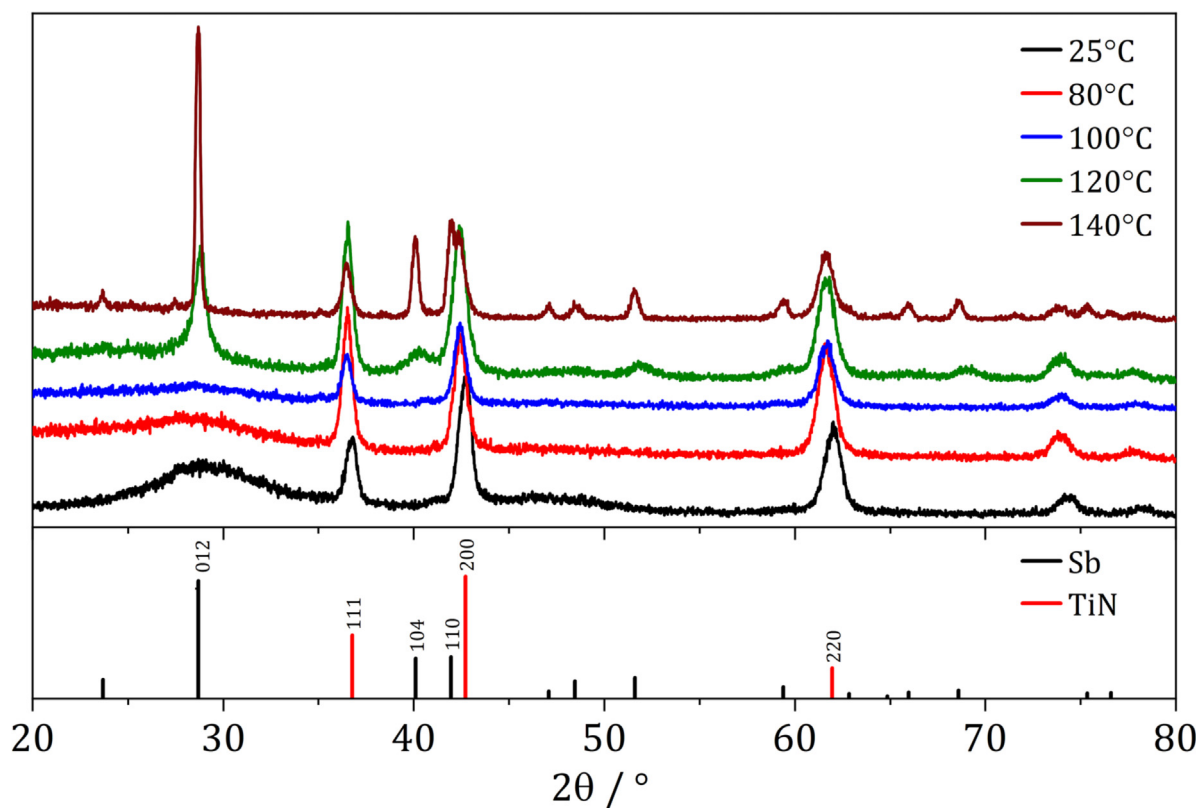| Temperature / °C	$j_{d,av}$ / μA cm^{-2}	$a = b$ / Å	c / Å	Average crystallite size / Å
25	43	4.25(5)	10.4(7)	11(1)[a]
80	578	4.36(15)	11.5(5)	22(2)[a]
100	791	4.27(14)	10.4(2)	23(3)[a]
120	878	4.24(4)	11.1(2)	94(24)[b]
140	488	4.31(1)	11.3(1)	233(30)[b]
Lit.[c]		4.31	11.3	

Fig. 4. XRD patterns of Sb electrodeposited on TiN at varying temperatures from oDCB containing 3 mM $[N^nBu_4][SbCl_4]$. Black: 25 °C, red: 80 °C, blue: 100 °C, green: 120 °C, brown: 140 °C. Bottom panel shows in black the literature pattern for Sb (ICSD 64695), and in red TiN (ICSD 152807). Offset is arbitrary and added for clarity. (For interpretation of the references to colour in this figure legend, the reader is referred to the web version of this article.)

Fig. 4 shows XRD patterns from the Sb deposited at each temperature. At 25 °C a single broad peak associated with the deposit can be observed at *ca.* 28°, which corresponds to the primary diffraction peak of elemental Sb. The calculated lattice parameters in Table 2 show good agreement with the literature values for Sb [21]. The shape of the peak suggests that the material is amorphous, as reported by Reeves *et al.* when deposited from DCM [11]. This is also indicated by the small average crystallite size estimated from the Scherrer equation, also in Table 2. Up to 100 °C the XRD pattern does not change significantly with increasing temperature, suggesting that whilst the morphology of the deposit is changing, the temperature is having a negligible effect on the crystallinity of the deposited Sb. This is also reflected in the average crystallite sizes, which remain effectively constant. At 120 °C however, a defined peak at 28° appears, and minor

diffraction peaks of Sb can also be observed. Then upon heating to 140 °C a far more intense peak occurs, and the large crystallite sizes indicate that Sb was deposited in a crystalline form.

Raman spectroscopy is complementary to XRD data. Raman active materials display peaks at positions unique to the material and therefore can be used to identify the presence of a particular material. Literature reports indicate that crystalline Sb shows Raman peaks at 115 cm^{-1} and 150 cm^{-1}, corresponding respectively to the TO and LO Raman modes [22]. Raman spectra of the collected Sb electrodeposits are shown in Fig. 5. For the deposits at 25, 80 and 100 °C, no such peaks occur, and instead a large broad peak with maxima at 143, 140 and 142 cm^{-1}, respectively are present in each spectrum, along with a smaller peak at *ca.* 80 cm^{-1}. Cheng *et al.* reported Raman spectra of amorphous antimony thin films which displayed a peak at approx. 145 cm^{-1} and a small hump at *ca.* 95 cm^{-1} [23], similar to that observed here. Since the expected peaks for crystalline antimony are not observed, this corroborates the evidence from XRD that the deposits are amorphous. At 120 °C, a peak is now present at 149 cm^{-1}, along with a shoulder at lower wavenumber, suggesting the presence of partially crystalline Sb. Finally at 140 °C, two peaks can be observed at 110 and 149 cm^{-1}, clearly showing the presence of crystalline Sb.

To summarise, on increasing the temperature from 25 to 140 °C for the electrodeposition of Sb the morphology of the deposit changes as seen by SEM and the deposit changes from amorphous to crystalline as determined by XRD and Raman.

3.3. Antimony telluride electrodeposition

Turning to the electrodeposition of Sb$_2$Te$_3$, Fig. 6 shows a voltammogram of a mixed Sb^{3+} and Te^{4+} electrolyte in oDCB. Scanning cathodically, reduction begins at ca. −1.2 V, similar to Sb in Fig. 1 above, therefore presumably corresponding to the onset of Sb deposition. An increase in reduction current then occurs, possibly indicating the start of Te deposition. On the reverse sweep little metal stripping appears to take place, as evidenced by the lack of oxidation current, as with Sb also. No significant changes to the voltammetry occur on subsequent scans.

Antimony telluride was electrodeposited at increased temperatures from oDCB containing 1.5 mM [N^{n}Bu$_4$][SbCl$_4$] and 3 mM [N^{n}Bu$_4$]$_2$[-TeCl$_6$]

Fig. 6. Voltammograms of 1.5 mM [N^{n}Bu$_4$][SbCl$_4$] and 3 mM [N^{n}Bu$_4$]$_2$[-TeCl$_6$] with 100 mM [N^{n}Bu$_4$]Cl at a 4 mm dia. TiN WE in oDCB at 25 °C. Scan swept from 0.5 V *vs.* Ag/AgCl at 100 mV s^{-1} in the direction indicated by the arrows. CE: Pt mesh, RE: Ag/AgCl.

TeCl$_6$] at −1.75 V *vs.* Ag/AgCl, conditions which gave stoichiometric Sb$_2$Te$_3$ at room temperature. Assuming once again that the overpotential for deposition does not change significantly with temperature.

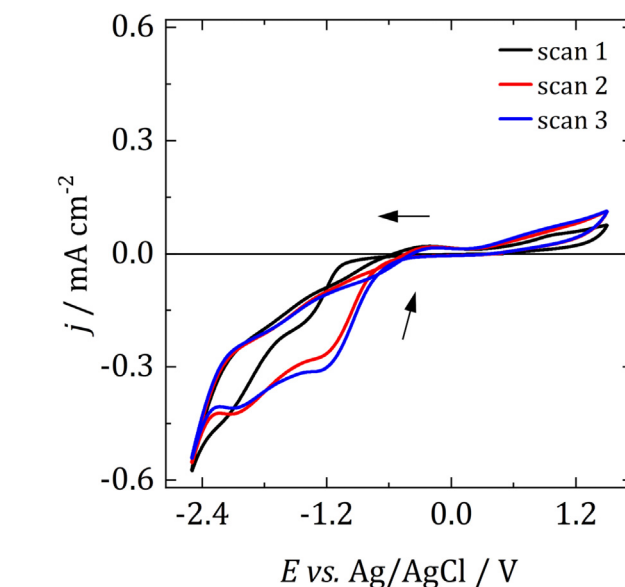Fig. 7 shows the effect of temperature on the composition of the resulting co-deposits. At 40 °C the composition remains unchanged from that at 25 °C, however as the temperature increases further, the Sb composition in the deposit decreases approximately linearly with temperature. Deposition was not attempted at temperatures > 120 °C due to the apparent decomposition of the electrolyte (see below).

Inspection of the Sb-Te phase diagram indicates that stoichiometric Sb$_2$Te$_3$ forms at a narrow composition range around 40% Sb [24]. For alloys with Sb compositions less than 40%, the additional Te precipitates as elemental Te. Meaning that the deposits collected at 80 and 120 °C are likely a combination of Sb$_2$Te$_3$ + Te.
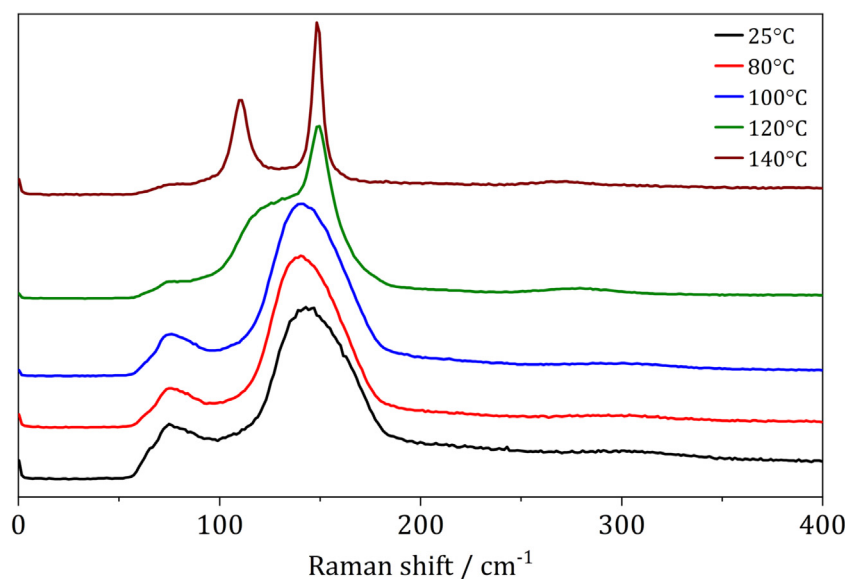
Fig. 5. Raman spectra of Sb electrodeposited at varying temperatures onto TiN from oDCB containing 3 mM [N^{n}Bu$_4$][SbCl$_4$]. Collected using 785 nm excitation laser and intensity normalised by y_{max}. Black: 25 °C, red: 80 °C, blue: 100 °C, green: 120 °C, brown: 140 °C. Offset is arbitrary and added for clarity. (For interpretation of the references to colour in this figure legend, the reader is referred to the web version of this article.)
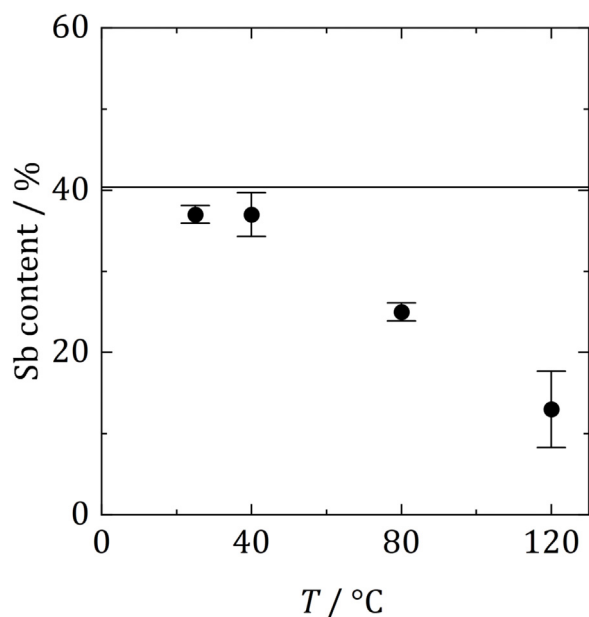
Fig. 7. The effect of temperature on the composition by EDX of antimony telluride electrodeposited onto TiN from oDCB containing 1.5 mM $[N^nBu_4]$ $[SbCl_4]$ and 3 mM $[N^nBu_4]_2[TeCl_6]$. Values are the average composition of three locations on the deposit and the error the standard deviation. Horizontal line indicates the composition of a commercial standard.

To investigate whether the change in deposit composition was directly caused by the change in temperature itself, or was an indirect result of another process such as precursor decomposition, the electrolyte was heated to 80 °C, then cooled back to 25 °C and a deposit collected. This was then repeated for 120 °C. Compositional analysis by EDX gave Sb content of 36 ± 2% and 36 ± 1% for the deposits heated to 80 °C and 120 °C respectively. The Sb/Te ratio is in agreement with that observed without heating, showing that the electrolyte is unaffected by being heated up to 120 °C. This is an important result because it indicates that the temperature is directly affecting the composition of the electrodeposited compound. It appears possible to rationalise this phenomenon in terms of Plieth's kinetic 'kink site' model [25]. This is based on the concept of residence times in so called kink sites. According to this model, during the process of alloy electrodeposition the reduced metal atoms pass through an intermediate stage where they reside at a kink site. Once at the kink site, the atom can become incorporated into the metal lattice by arrival of more reduced atoms or it can separate from the kink site and return to the electrolyte. The arriving atom can be the same as, or different from, the atom residing in the kink site and the residence time is then defined as the average time that the new atom spends in each of the possible kink sites. If the residence time of the newly reduced atom is longer in a kink site with a native atom than in a kink site with its counterpart in the alloy, then a solid solution forms. If the opposite is true, alloy or compound formation is favoured. The ratios of the different residence times then give an indication of the relative preference of an atom for association with itself. In the Sb/Te system studied here, it is possible that the residence times of the reduced Sb and Te atoms are changing with temperature. The results are consistent with the residence time of the Te atom in a Te kink site increasing relative to its residence time in a Sb kink site with increasing temperature.

Despite changes in the composition of the deposits, they appear to display improvements in their material properties. The morphology of the deposits become smoother and more uniform with increasing temperature in a similar fashion to Sb above, as evidenced by SEM images in Fig. 8. Up to 80 °C, the deposits appear as isolated clumps of mate-

rial on the substrate, whereas at 120 °C a uniform and continuous film forms.

The deposits were additionally studied with XRD, with patterns shown in Fig. 9. Sb_2Te_3 and Te have major diffraction peaks in similar positions meaning that it is not possible to distinguish the diffraction of Sb_2Te_3 from the signal arising from the additional elemental Te in the deposit. The patterns were indexed with both antimony telluride and tellurium, with the calculated lattice parameters of Sb_2Te_3 given in Table 3. Also shown in Table 3 are the average crystallite sizes from the peaks. These become larger with increasing temperature, suggesting that the crystallinity of the electrodeposited material improves when deposited at increased temperatures.

### 3.4. The effect of temperature on deposit roughness

Inspection of the SEM images of the deposited Sb and Sb_xTe_y in Figs. 3 and 8 above show that, qualitatively, they appear to become smoother with increasing temperature. For certain applications, such as in bright nickel, tin or chromium electroplating for decorative purposes, having smooth metal films is a highly desirable property and is usually achieved with use of addititives [26]. The extended depth of focus (EDF) feature of an optical microscope was used to study this further and attempt quantitative analysis. An EDF image is obtained by capturing images at several distances along the z axis which are then stitched together to form a single image where the entire surface is in focus at all distances in the z direction. A common approach to roughness measurements is with atomic force microscopy (AFM) or profilometers such as a digital holographic microscope. These approaches require equipment far more specialised than a simple optical microscope and, in the case of AFM, only sample a small area that is not necessary representative of the entire surface of the material. EDF images were obtained for Sb and Sb_xTe_y samples deposited at 25 and 120 °C in representative locations, with a z axis resolution of 50 nm. The as collected images are given in Figs. S4–S7, these can then be converted into 3D height maps which are shown in Figs. S8–S11. The EDF images sample an area of 4000–5000 μm^2, much greater than the 10–100 μm^2 measured using AFM. Use of optical methods naturally also come with a loss in resolution, however it is still possible to observe macroscale changes in the surface of the deposits.

A cross-sectional z profile can also be obtained from the EDF images, shown in Fig. 10. This gives an indication of the change in height across the surface of the deposits. A plane representative of the whole EDF image was chosen as the location for the cross-section. Qualitatively, it is clear that there is significantly less variation for both Sb and Sb_xTe_y when deposited at elevated temperatures. The standard deviation of the average heights, σ, along with the differences, Δz, between the maximum and minimum points in the profile are given in Table 4. As can be seen, both decrease by approximately a factor of 4 for Sb and Sb_xTe_y as a result of increasing the deposition temperature, demonstrating that electrodeposition at elevated temperatures does indeed lead to smoother deposits, and quantitatively supporting the conclusions implied by the SEM images in Figs. 3 and 7.

3.5. The effect of temperature on the chemistry of the electrolyte

Since there was evidence to suggest changes in the nature of the electrolyte components with temperature (see above), the stability of the electrolyte components was studied to investigate the effect of temperature on their chemistry. Individual solutions of 100 $[N^nBu_4]$ Cl, 3 mM $[N^nBu_4][SbCl_4]$ and 3 mM $[N^nBu_4]_2[TeCl_6]$ in oDCB were prepared, heated to 140 °C, and then analysed.

For the solution of $[N^nBu_4]Cl$, mass spectrometric (MS) analysis was performed after heating. The results indicated the presence of $[N^n-Bu_4]^+$ as expected, but also $[N^nHBu_3]^+$. This could have formed as a result of a Hoffmann elimination of the $[N^nBu_4]^+$ cation, with the pro-
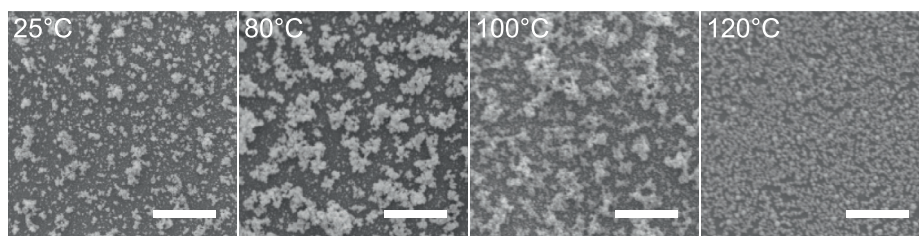
Fig. 8. SEM images of Sb_xTe_y deposited at varying temperatures onto a TiN substrate from oDCB containing 1.5 mM $[N^nBu_4][SbCl_4]$ and 3 mM $[N^nBu_4]_2[TeCl_6]$. Scale bar represents 10 μm.
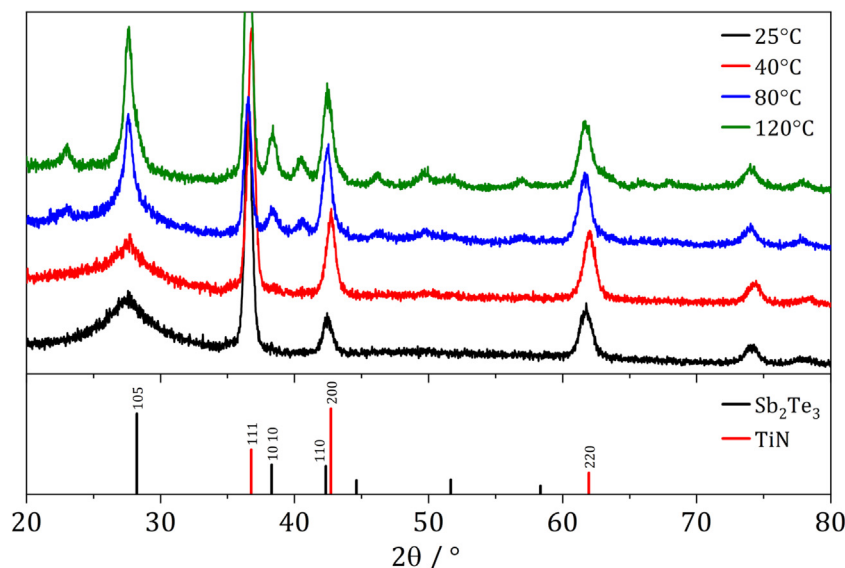
Fig. 9. XRD patterns of antimony telluride electrodeposited at various temperatures onto TiN from oDCB containing 1.5 mM $[N^nBu_4][SbCl_4]$ and 3 mM $[N^nBu_4]_2[TeCl_6]$. Black: 25 °C, red: 40 °C, blue: 80 °C, green: 120 °C. Bottom panel shows in black the literature pattern for Sb_2Te_3 (ICSD 2084) and in red TiN (ICSD 152087). (For interpretation of the references to colour in this figure legend, the reader is referred to the web version of this article.)
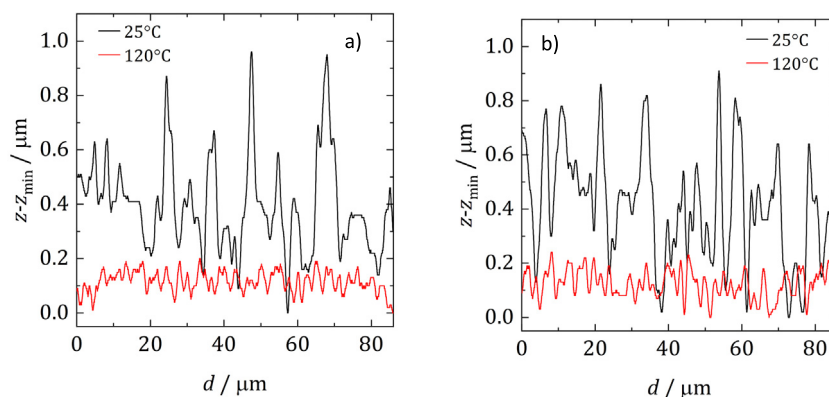
Table 3
Growth rate and crystal structures refined from XRD patterns of antimony telluride electrodeposited at various temperatures onto TiN from oDCB. [a] ICSD 2084. [b] calculated using the Scherrer method. [c] calculated using the Halder-Wagner method.

Temperature / °C	$j_{d,av}$ /μA cm^{-2}	$a = b$ / Å	c / Å	Average crystallite size / Å
25	5	4.28(4)	31.1(3)	21(3)[b]
40	30	4.23(6)	30.7(4)	23(1)[b]
80	82	4.28(2)	30.2(2)	55(3)[c]
120	213	4.28(2)	30.8(1)	56(12)[c]
Lit.[a]		4.26	30.5	

ton possibly originating from the ionisation process, and suggests the supporting electrolyte decomposes at the highest temperatures.

With $[N^nBu_4][SbCl_4]$, whilst the Sb-121 isotope is NMR active, its large quadrupole moment means that other than in a spherically symmetrical environment (such as the $[SbCl_4]^-$ anion itself), fast quadrupolar relaxation usually results in resonances not being observable. As such, there are no readily available methods of directly studying the metal centre as a function of temperature. Instead, an indirect electrochemical approach was used. Voltammograms were recorded, and electrodeposition attempted, before and after heating to 140 °C. Fig. 11 shows CVs at a TiN WE of the electrolyte at 25 °C with no prior heating, at 140 °C, and upon cooling the cell back to 25 °C. The initial voltammogram appears similar to that in Fig. 1 above, as would be expected. At 140 °C, reduction and oxidation are present, which are presumably still the deposition and stripping of Sb, however the definition of the peaks is lost. Finally, when the electrolyte was cooled

back to 25 °C the voltammogram appeared significantly different from the CV of a sample that had not been heated. There was no evidence of any material on the electrode surface by SEM (Fig. S12), indicating that heating to 140 °C causes irreversible changes to the Sb precursor, which ultimately prevents its electrodeposition. To demonstrate that the effect is directly associated with the $[SbCl_4]^-$ precursor, an electrolyte containing 100 mM $[N^nBu_4]Cl$ and oDCB was heated to 140 °C, cooled to 25 °C and then 3 mM $[N^nBu_4][SbCl_4]$ was added. The subsequent voltammogram and SEM image of the resulting deposit are shown in Fig. S13. Interestingly, both the voltammogram and the deposit morphology appear to differ from an unheated electrolyte, perhaps associated with the reactions of the supporting electrolyte above. Nevertheless, a nucleation loop can be observed, indicative of the redox active Sb^{3+} species, and the electrodeposition of elemental Sb is still possible. The exact mechanism of the decomposition of $[SbCl_4]^-$ is difficult to ascertain. The Sb-species in the electrolyte is soluble;

Fig. 10. Cross-sectional z profile of a) Sb and b) Sb_xTe_y electrodeposited at 25 °C and 120 °C from oDCB. Obtained from an optical extended depth of focus image with a z resolution of 50 nm. Height is normalised by the minimum value of each profile.

Table 4
Effect of temperature on quantitative measurements of the height profile of electrodeposited Sb and Sb_xTe_y from oDCB. [a] standard deviation of the average height from a segment of the deposit. [b] difference between maximum and minimum points.

	Temperature / °C	σ^a / μm	Δz^b / μm
Sb	25	0.17	0.96
	120	0.04	0.20
Sb_xTe_y	25	0.21	0.96
	120	0.05	0.24
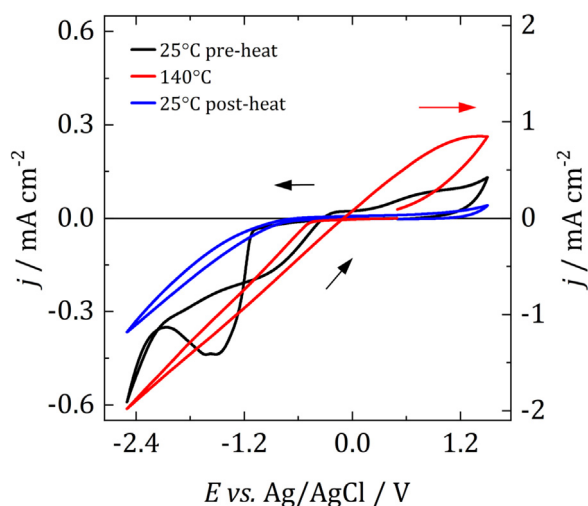
Fig. 11. The effect of heating on voltammograms of 3 mM $[N^nBu_4][SbCl_4]$ and 100 mM $[N^nBu_4]Cl$ at a 4 mm dia. TiN in oDCB. Scan swept from 0.5 V *vs.* Ag/AgCl at 100 mV s^{-1} in the direction indicated by the arrows. CE: Pt mesh, RE: Ag/AgCl.

since no precipitate was observed, but is not redox-active, as no significant quantity of elemental Sb can be electrodeposited from it.

Finally, $[N^nBu_4]_2[TeCl_6]$ was observed to decompose at temperatures above 120 °C. A black precipitate formed which, when removed for further analysis, was confirmed by EDX analysis to be elemental Te. A representative SEM image and EDX spectrum can be found in Fig. S14. Te^{4+} in solution appears to be reduced to Te^0, although it is not clear what the reducing agent is.

4. Conclusions

oDCB was used to study the effect of temperature on the electrodeposition of antimony and antimony telluride. SEM images indicated that the deposits became smoother and more homogeneous as the temperature increased. Deposition at higher temperatures also improved the crystallinity of the resulting deposits, as evidenced by XRD analysis.

The antimony content in antimony telluride co-deposits decreased with increasing temperature, and it was no longer possible to electrodeposit stoichiometric Sb_2Te_3. This was attributed to changes in the relative affinity of freshly reduced Sb and Te atoms for themselves or the complementary metal in the alloy with temperature. Since the electrolyte remains unaffected by temperature up to 120 °C, in principle it will be possible in the future to optimise the ratio of the precursor concentrations for a given temperature. This will permit the electrodeposition of stoichiometric material with the additional benefits of using elevated temperatures.

At the highest applied temperature of 140 °C, the $[SbCl_4]^-$ anion appeared to decompose, which affected its ability to electrodeposit Sb. This also appeared to cause a change in the morphology of the deposited material. This may limit the broader applicability of this electrolyte system for the electrodeposition of crystalline semiconductors.

Finally, for a given material it remains unclear on a microscopic level why exactly increasing the operating temperature causes a change from deposition of amorphous materials to crystalline materials and over what temperature range this transition will take place. There does not appear to be a satisfactory explanation for this phenomenon in the literature. It may, however, be possible to gain insight from knowledge on the mechanisms of crystallisation [27]. Here, the transition from amorphous to crystalline is treated as a thermally-activated process, meaning the rate of crystallisation follows an Arrhenius type relationship with an associated activation energy of crystallisation [28]. Therefore when the bath temperature is increased, a greater proportion of the reduced atoms are able to overcome the activation energy of crystallisation and so the deposit adopts a crystalline form.

CRediT authorship contribution statement

Alexander W. Black: Conceptualization, Methodology, Validation, Formal analysis, Investigation, Data curation, Writing – original draft, Visualization. **Wenjian Zhang:** Methodology, Resources. **Yasir J. Noori:** Methodology, Validation, Resources. **Gillian Reid:** Methodology, Conceptualization, Resources, Writing – review & editing, Supervision. **Philip N. Bartlett:** Conceptualization, Methodology,

Validation, Formal analysis, Writing – review & editing, Supervision, Funding acquisition, Project administration.

Declaration of Competing Interest

The authors declare that they have no known competing financial interests or personal relationships that could have appeared to influence the work reported in this paper.

Acknowledgements

Appendix A. Supplementary data

Supplementary data to this article can be found online at https://doi.org/10.1016/j.jelechem.2023.117638.

References

[1] K. Cicvarić, L. Meng, D.W. Newbrook, R. Huang, S. Ye, W. Zhang, A.L. Hector, G. Reid, P.N. Bartlett, C.H.K. De Groot, ACS Omega 5 (2020) 14679–14688.

[2] G.P. Kissling, M. Aziz, A.W. Lodge, W. Zhang, M. Alibouri, R. Huang, A.L. Hector, G. Reid, C.H. de Groot, R. Beanland, P.N. Bartlett, D.C. Smith, J. Electrochem. Soc. 165 (2018) D802–D807.

[3] Y.J. Noori, L. Meng, A.H. Jaafar, W. Zhang, G.P. Kissling, Y. Han, N. Abdelazim, M. Alibouri, K. Leblanc, N. Zhelev, R. Huang, R. Beanland, D.C. Smith, G. Reid, K. De Groot, P.N. Bartlett, ACS Appl. Electron. Mater. 3 (2021) 3610–3618.

[4] A.W. Black, P.N. Bartlett, Phys. Chem. Chem. Phys. 24 (2022) 8093–8103.

[5] J. Gu, E. Fahrenkrug, S. Maldonado, J. Am. Chem. Soc. 135 (2013) 1684–1687.

[6] W. Wu, N. Eliaz, E. Gileadi, J. Electrochem. Soc. 162 (2015) D20–D26.

[7] S. Murugesan, A. Akkineni, B.P. Chou, M.S. Glaz, D.A. Vanden Bout, K.J. Stevenson, ACS Nano 7 (2013) 8199–8205.

[8] S. Thomas, D.E. Smith, V.K. Greenacre, Y.J. Noori, A.L. Hector, C.H. de Groot, G. Reid, P.N. Bartlett, J. Electrochem. Soc. 167 (2020) 106511.

[9] J. Cao, Y. Wu, H. Zhang, D. Logoteta, S. Zhang and M. Pala, *npj 2D Mater. Appl.*, **5**, 59.

[10] J.H. Sung, H. Heo, I. Hwang, M. Lim, D. Lee, K. Kang, H.C. Choi, J.H. Park, S.H. Jhi, M.H. Jo, Nano Lett. 14 (2014) 4030–4035.

[11] S.J. Reeves, Y.J. Noori, W. Zhang, G. Reid, P.N. Bartlett, Electrochim. Acta 354 (2020) 136692.

[12] K. Cicvarić, PhD thesis, University of Southampton, 2020.

[13] P.N. Bartlett, D. Cook, C. H. (Kees) de Groot, A. L. Hector, R. Huang, A. Jolleys, G. P. Kissling, W. Levason, S. J. Pearce and G. Reid,, RSC Adv. 3 (2013) 15645–15654.

[14] E.L. Yee, R.J. Cave, K.L. Guyer, P.D. Tyma, M.J. Weaver, J. Am. Chem. Soc. 101 (1979) 1131–1137.

[15] A.J. deBethune, T.S. Licht, N. Swendeman, J. Electrochem. Soc. 106 (1959) 616–625.

[16] S. Sahami, M.J. Weaver, J. Electroanal. Chem. 122 (1981) 155–170.

[17] D. Tran, J.P. Hunt, S. Wherland, Inorg. Chem. 31 (1992) 2460–2464.

[18] M. Matsumoto, T.W. Swaddle, Inorg. Chem. 43 (2004) 2724–2735.

[19] W.M. Haynes, D.R. Lide, T.J. Bruno, CRC Handbook of Chemistry and Physics, 96th edn., CRC Press, New York, 2016.

[20] I. Noviandri, K.N. Brown, D.S. Fleming, P.T. Gulyas, P.A. Lay, A.F. Masters, L. Phillips, J. Phys. Chem. B 103 (1999) 6713–6722.

[21] C.S. Barrett, P. Cucka, K. Haefner, Acta Crystallogr. 16 (1963) 451–453.

[22] P.N. Bartlett, J. Burt, D.A. Cook, C.Y. Cummings, M.W. George, A.L. Hector, M.M. Hasan, J. Ke, W. Levason, D. Pugh, G. Reid, P.W. Richardson, D.C. Smith, J. Spencer, N. Suleiman, W. Zhang, Chem. A Eur. J. 22 (2016) 302–309.

[23] Z. Cheng, T. Milne, P. Salter, J.S. Kim, S. Humphrey, M. Booth, H. Bhaskaran, Sci. Adv. 7 (2021) 1–10.

[24] G. Ghosh, J. Phase Equilibria 15 (1994) 349–360.

[25] W. Plieth, in *Electrochemistry for Materials Science*, Elsevier, Amsterdam, 2008, pp. 231–262.

[26] M. Schlesinger, M. Paunovic, Modern Electroplating, 5th ed., Wiley, Hoboken, NJ, 2010.

[27] W. Beckmann, Crystallization, Wiley-VCH Verlag GmbH, Weinheim, 2013.

[28] N. Mehta, A. Kumar, J. Phys. Chem. B 120 (2016) 1175–1182.